Computational and experimental design of active and durable Ir-based nanoalloy for electrochemical oxygen reduction reaction

Jinwon Cho[a], Injoon Jang[a], Hyun S. Park[a,b], Sun Hee Choi[a,b], Jong Hyun Jang[a,b,c], Hyoung Juhn Kim[a,b], Sung Pil Yoon[a,b], Sung Jong Yoo[a,b,*], Hyung Chul Ham[a,b,*]

[a] Fuel Cell Research Center, Korea Institute of Science and Technology (KIST), Hwarangno 14-gil 5, Seongbuk-gu, Seoul, 02792, Republic of Korea
[b] Division of Energy & Environment Technology, KIST School, Korea University of Science and Technology (UST), Seoul, 02792, Republic of Korea
[c] Green School, Korea University, Anam-ro 145, Seongbuk-gu, Seoul, 02841, Republic of Korea

ABSTRACT

Despite recent efforts on replacing a noble Pt to less expensive catalysts (such as Pt-Ni and Pt-Co alloys) for improving oxygen reduction reaction (ORR) for PEMFC (polymer electrolyte membrane fuel cell) application, the performance and stability of a noble Pt catalyst still remains superior. In the present study, we have proposed the systematic procedure for designing the Ir_3M (M = 3d, 4 d, 5 d transition metal) nanoalloy as Pt alternatives with enhanced ORR activity and stability using density functional theory (DFT) and experimental methods.

First, we computationally optimized the surface occupied/unoccupied d states and lattice distance of the thermodynamically-stable Ir_3M nanoalloy in order to achieve the wanted oxygen affinity for promoting ORR. In the next screening process, the nanoalloy prone to the segregation of inside M atom toward the surface layer was excluded, leading ultimately to the potential candidates such as the pure Ir monolayer on the top of Ir_3Cr, Ir_3V, Ir_3Re, and Ir_3Tc alloy cores. Finally, a pure Ir monolayer on the top of Ir_3Cr core (which was expected to show the most enhanced ORR activity among the computationally-screened candidates) was experimentally prepared via physical vapor deposition method (PVD) and electrochemically evaluated for confirming our DFT prediction. Our synthesis successfully produced a 3 nm Ir-covered (so-called Ir skinlayer) Ir_3Cr nanoparticle (Ir/Ir_3Cr), which displayed the surface lattice contraction by 1.03% compared to the pure Ir case. The specific activity (at 0.7 V vs RHE) of a Ir/Ir_3Cr catalyst with the very high durability (showing only 0.05% decrease from the initial activity after 3000 potential cycles) was 12.3 times higher than a Ir catalyst. The detail mechanism on the enhanced activity in Ir-M alloy was also examined. The design principle of alloy catalysts used in this study can be further extended to the screening of catalytic materials for the application to the next-level electrochemical reaction.

1. Introduction

Proton exchange membrane fuel cells (PEMFCs) are considered as promising sources of green energy in the mobile and consumer electronic industries because of their highly efficient energy conversion rate, power density, and environmentally toxic free products [1–3]. Throughout the years, a number of researches have been conducted in aim to develop cost-effective PEMFCs; nonetheless, replacing high priced platinum(Pt) catalyst in PEMFC system to economical and efficient catalyst still remains challenging to the commercialization of energy conversion devices.

Recent studies on oxygen reduction reaction (ORR) catalysts in PEMFC have attempted to replace Pt with the noble Au, Ag, and Pd-based alloys [1,4–15]. Although such catalysts have been found to

improve the ORR activity, the best ORR catalysts still remain Pt-based catalysts because of the fast degradation of catalytic materials at acidic cathode condition [1].

The next available option to increase the stability of catalysts in fuel cell condition is Iridium (Ir) based alloy catalysts [16]. Iridium is considered as a potential candidate for ORR catalysts for its high stability in the acidic medium. However, Ir catalyst suffers from the low ORR activity in comparison with Pt catalyst [17,18]. In order to overcome such activity issue of Ir catalyst, Ir-based binary or ternary alloys have been studied [18]. For example, the previous experimental studies have showed that Ir–M (M: Sc, V, Co, Sn, Ru) alloys have potential to be efficient ORR catalysts in fuel cells [17,18].

During the ORR process, various adsorbates, such as O and OH are formed and they have been reported to accumulate on the surface as

ORR intermediates [19,20]. In case where these adsorbates remain on the surface, it is more likely that Ir-M catalysts are energetically favorable to have surface segregation [18]. For instance, during the extensive operation of fuel cell, Co atoms in Ir-Co catalyst tend to dissolve into the electrolyte and ultimately the longevity of catalyst is decreased due to the unwanted Co products [18,21]. These adsorbates lead to leaching of the alloy solute from the catalyst surface into the electrolyte [18,21,22]. Therefore, searching for Ir-M alloy catalysts where a solute metal is energetically favored to remain unchanged in alloy catalyst when the surface is exposed to adsorbed ORR species is significant. As a solution, the formation of pure Ir surface (so-called Ir-skinlayer) by selectively removing the solute M atom near the surface region in Ir-M alloy catalyst is suggested to improve the stability of Ir-M catalysts [1,18,19,23]. Thereby, in this work, we conducted the systematic density functional theory (DFT) calculations by computationally modelling Ir_3M (M is 3 d, 4 d, 5 d transition metals) bimetallic alloy catalysts and Ir-skinlayer on the top of Ir_3M to discover the catalyst with improved ORR catalytic activity and stability. The underlying mechanisms that control surface reactivity in Ir_3M alloy catalyst were also studied in detail via the theoretical analysis. Finally, the selected candidate was experimentally prepared and evaluated under the electrochemical conditions in order to confirm the accuracy of DFT-based prediction on the activity and stability of electrocatalyst. This study can highlight the scientific insight for designing bimetallic catalysts for next-level electrochemical reduction.

2. Methods

2.1. Computational methodology

The Calculations performed herein was on the basis of DFT using the generalized gradient approximation (GGA) of the PW91 for exchange-correlation as implemented in the Vienna Ab-initio Simulation Package (VASP) [24,25]. The description of the interaction between the core and valence electrons was employed by projector augmented wave (PAW) method with a planewave basis set [26] where the cutoff energy for the planewave expansion of the electronic eigenfunctions was 350 eV.

The Gibbs free energy per atom for forming a bulk Ir_3M(M = 3d, 4 d, and 5 d metals) alloy [defined as ΔG_{form}] at T = 323 K was calculated by the following equation.

$$\Delta G_{form} = \frac{1}{4} \times [G(Ir_3M) - 3 \times G(Ir) - G(M)] \qquad (1)$$

Where $G(Ir_3M)$ is the Gibbs free energy per atom of the bulk Ir_3M alloy, $G(Ir)$ is the Gibbs free energy per atom of the pure bulk Ir element, and $G(M)$ is the Gibbs free energy per atom of the pure bulk M element. Here, Gibbs free energy was determined by considering the zero-point energy(ZPE) and entropy (S) using the following equations.

$$S = k_B \sum_{i}^{\# \, of \, modes} \left\{ \frac{x_i}{e^{x_i}-1} - \ln(1-e^{-x_i}) \right\} \qquad (2)$$

$$x_i = \frac{h\nu_i}{k_B T} \qquad (3)$$

$$ZPE = \sum_{i} \frac{1}{2} h\nu_i$$

Where k_B, h and x_i is the Boltzmann constant, Planck's constant and vibrational mode in terms of vibrational frequency, ν_i, respectively.

For model surfaces, we used the (2 × 2) five-layer fcc(111) slabs (see Fig. 1) with calculated equilibrium lattice constants (see Table S1) to model the Ir_3M surfaces where the bottom two layers are fixed to simulate the core of catalyst and the rest are relaxed for optimization by adopting the conjugate gradient method until remaining forces on all the constituents of the atom become smaller than 5×10^{-2} eV/Å. Since the slab model is separated from its periodic images in order to avoid the interaction between the top surface and the bottom of periodic

images in the vertical direction, vacuum layers equivalent to seven atomic layers were applied. The Monkhorst-Pack mesh of k points (5 × 5 × 1) was also implemented for the Brillouin zone integration to optimize structural geometries and the corresponding total energies. Then, for the calculation of the electronic structure calculation and the Bader charge analysis, the Monkhorst-Pack mesh the k points was increased to (12 × 12 × 1) to understand the charge flow between alloying components.

The oxygen binding (adsorption) energy is given by the following equation [27].

$$E_{b,O} = E_{bare/O} - E_{bare} - \frac{1}{2}E_{O2} \qquad (4)$$

Where, $E_{bare/O}$, E_{bare} and E_{O2} represent the total energy of the oxygen-adsorbed slab, the clean slab and the triplet state O_2 at gas phase, respectively

2.2. Synthetic methods and characterization

2.2.1. Preparation of NP/glucose

The synthesis of Ir/C and Ir_3Cr/C was followed in our previous study [27]. Detailed methods are as follows: Using a radio-frequency (RF) magnetron sputter system under an Ar atmosphere, Ir nanoparticles(NPs) were directly deposited on the glucose surface. Glucose anhydrous powder (Sigma-Aldich, 96%) was placed in a specially designed vessel to mix the powder, and was stirred during sputter process. Co-sputtering technique that simultaneously deposit multi targets onto substrate was used to deposit the Ir_3Cr alloy NPs on the glucose. The base pressure and the working pressure were maintained at < 2 $\times 10^{-6}$ Torr and 5 mTorr, respectively, for all sputter processes that deposited the nanoparticles on the glucose. The sputter powers of Ir and Cr were 20 W and 15 W, respectively, and the target was 20 cm away from glucose substrate.

2.2.2. Synthesis of NP/C

The process of synthesizing carbon-supported Ir or Ir/Ir_3Cr from Ir/Glu and Ir_3Cr/Glu is as follows. Commercial carbon (Vulcan XC-72R, Cabot Co., BET: 237 m²/g, denoted as C) was dispersed into purified DI water (250 mL) using ultra-sonication at room temperature for 30 min. A calculated amount of Ir/Glu or Ir_3Cr/Glu powder was added into the carbon-dispersed DI water. The resulting solution was stirred at 80 °C for 3 h and further stirring was carried out at room temperature for about 12 h for high transfer of the nanoparticles to the carbon surface. The final product was filtered, washed with DI water and dried overnight at 60 °C. Acid treatment was carried out for 12 h in 0.1 M $HClO_4$ solution at 60 °C to form Ir skin layer of Ir_3Cr/C. The Ir/C and $Ir/Ir_3Cr/$ C were calcined under 2 steps: i) 180 °C for 1 h in air to remove residue glucose; ii) 400 °C (Ir/C) or 750 °C ($Ir/Ir_3Cr/C$) for 1 h in H_2(5%)/Ar (95%) gas to reduce from IrO_x to Ir and better alloying of Ir_3Cr.

2.2.3. Physical characterization

TEM analysis was conducted with an FEI Titan™ 80–300 microscope operated at 300 kV. We used a JEOL ARM200F microscope for elemental analysis with EDX. Dmax2500/PC (Rigaku Co.) was used for XRD measurements scanning 2θ between 20° and 90° at 2° min⁻¹ and its X-ray radiation source is Cu Kα (k = 1.54056 Å) operating at 40 kV and 200 mA.

2.3. Electrochemical analysis

2.3.1. Preparation of catalyst coated glassy carbon electrode

The catalyst layer was obtained as follows: (i) first, a slurry was prepared by ultrasonic agitation of a mixture of 800 μL of DI water, 10 mg of catalyst, and 60 μL of Nafion solution (Aldrich: 5 wt% Nafion) for 10 min; (ii) second, 5 μL of the slurry was dropped on the carbon disc; (iii) third, the electrode was dried at room temperature for 10 min.
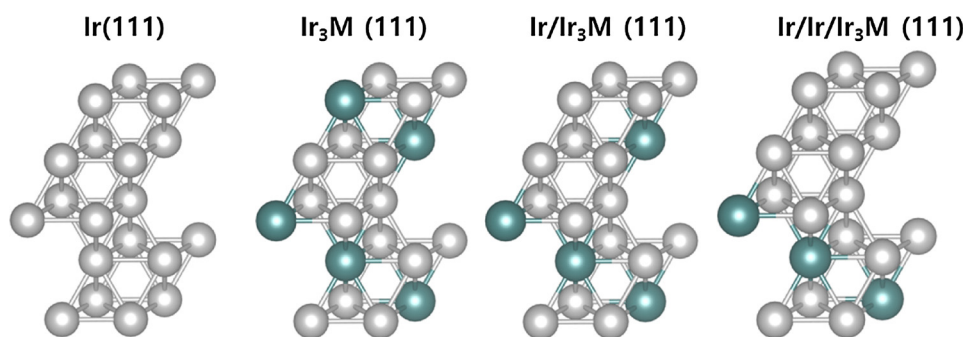
Fig. 1. The surface models used in this study. From left, a pure Ir(111) surface [denoted by Ir (111)], a bulk-terminated surface of $Ir_3M(111)$ slab [$Ir_3M/Ir_3M(111)$], a pure Ir monolayer supported on the surface of bulk-terminated $Ir_3M(111)$ slab [Ir/ $Ir_3M/Ir_3M(111)$], and a pure Ir bilayer on the surface of bulk-terminated $Ir_3M(111)$ slab [Ir/Ir/$Ir_3M(111)$]. Ir and M atoms are shown in grey and green color, respectively. (For interpretation of the references to color in this figure legend, the reader is referred to the web version of this article).

2.3.2. Oxygen reduction reaction (ORR) polarization

Prior to measuring ORR polarization curves, multiple cyclic voltammetry (CV) was carried out in deaerated 0.5 M H_2SO_4 solution at the can rate of $50\,mV\,s^{-1}$ in a potential window of 0.05–1.0 V vs RHE, at room temperature. The ORR activity was evaluated by the rotating disk electrode (RDE) technique in O_2-saturated 0.5 M H_2SO_4 solution with a sweep rate of $5\,mV\,s^{-1}$ at 1600 rpm, at room temperature.

3. Results and discussion

3.1. Formation energy of bulk Ir_3M alloy

The clear understanding of structure and composition in the alloy catalyst is essential for determining the catalytic activity. In particular, the distribution of alloy components at the surface and substrate is one of important factors that can significantly affect the surface reactivity of alloy catalysts since the interatomic mixing between alloy components can modify the activity of surface, and thus it is necessary to scrutinize the bulk composition of alloy catalyst and surface structure [23].

For such purpose, we first attempted to determine the Gibbs free energy per atom for forming a bulk $Ir_3M(M = 3d, 4\,d,$ and 5 d metals) alloy [ΔG_{form}] to filter out energetically unfavorable alloy composition. Here, $\Delta G_{form} < 0$ eV means that Ir_3M is thermodynamically stable and energetically favorable toward the formation of bulk alloy [28].

Fig. 2 displays the color-coded matrix of the formation energy for Ir_3M alloy (the exact values are provided in Table S1). Here, the deeper the red becomes, the higher the exothermicity of ΔG_{form} is. First, we see the endothermic ΔG_{form} (0.024–0.356 eV) for the Mn, Fe, Co, Ni, Cu, and Zn elements among 3d metals, whereas for the Sc, Ti, V, and Cr cases, the opposite is true ($\Delta G_{form} = -0.075$ to –0.55 eV), indicating that the early transition elements tend to form alloy with Ir element. For the 4d metal cases, our calculation predicts that the Ru, Rh, Pd, Ag and Cd elements are not capable of forming alloy with Ir since the ΔG_{form} of Ru, Rh, Pd, Ag, and Cd is higher than 0 eV with a value of 0.059 eV, 0.278 eV, 0.305 eV, 0.560 eV and 0.350 eV respectively. On the other hand, the Y, Zr, Nb, Mo, and Tc elements are calculated to be energetically favorable toward the formation of Ir_3M alloy. Looking at

the 5 d metal group, we find the stable alloy formation of the Lu, Hf, Ta, W, and Re elements with Ir, while for Os, Ir, Pt, Au, and Hg cases, the alloy formation is not energetically unfavorable.

3.2. Surface activity of Ir_3M alloy catalysts

From earlier studies, it has been reported that the oxygen binding energy plays as a key descriptor in understanding the ORR activity [29]. It has been well-established in the literature that the next available noble Ir (or Pd) catalyst with the high oxygen affinity improves the O_2 dissociation but hinders the formation of OH and H_2O from the dissociated O fragment and proton [27]. Thus, oxygen adsorption energy is a useful descriptor for the ORR activity of Ir-based alloys [27,28]. If the adsorption energy of O atom on stable alloy catalysts is higher than that of pure Ir, the increased ORR performance is expected for alloy catalysts [1,23,27,28].

In this section, we investigate the binding energies of oxygen atom [$E_{b,O}$] on the surface of thermodynamically stable Ir_3M alloy catalysts whose bulk formation energy is calculated to be exothermic (in previous section, we have found that the Sc, Ti, V, Cr, Y, Zr, Nb, Mo, Tc, Lu, Hf, Ta, W, and Re can form alloy with Ir).

For the clear understanding of the surface activity of Ir_3M alloy catalysts, three kinds of surface structures were examined as shown in Fig. 1. That is, (1) the bulk-terminated surface of $Ir_3M(111)$ [indicated by $Ir_3M/Ir_3M(111)$], (2) the pure Ir monolayer supported on the surface of bulk-terminated $Ir_3M(111)$ slab [indicated by Ir/ $Ir_3M/Ir_3M(111)$], and (3) the pure Ir bilayer on the surface of bulk-terminated $Ir_3M(111)$ slab [indicated by Ir/Ir/$Ir_3M(111)$]. Here, the pure Ir atomic layers in the near surface region of $Ir_3M(111)$ slab are called the Ir-*skinlayer*, which may be expected to significantly alter the surface reactivity and stability of catalysts. For example, Zhang et al. insisted that if alloy nanoparticles were configured as thin skinlayers of noble metals surrounded by non-noble metals, the skinlayers should be much more durable and efficient for ORR under fuel cell operating conditions [30,31].

As displayed in Fig. 3, for the bulk-terminated surface of $Ir_3M(111)$ [indicated by $Ir_3M/Ir_3M(111)$], our DFT calculation predicts the lower
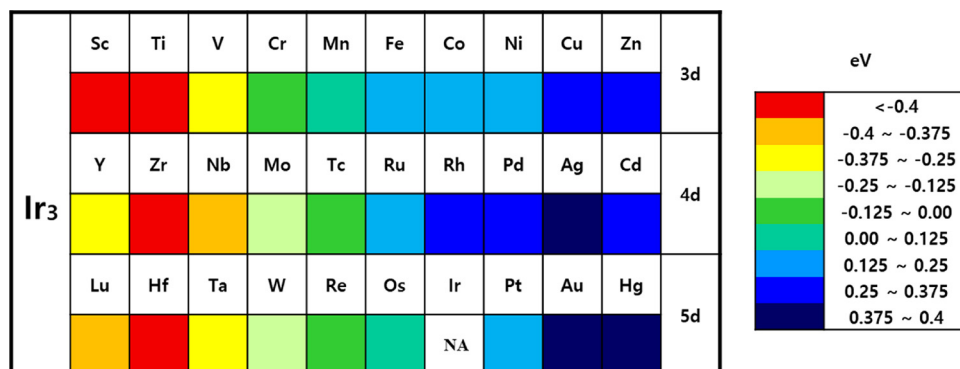

Fig. 2. The color-coded matrix of the Gibbs free energy per atom for forming a bulk Ir_3M (M = 3d, 4 d, and 5 d metals) alloy at T = 323 K. As color turns from bluegreen to blue, the formation energy becomes energetically unfavorable toward forming alloy structure, whereas for the color change from green to red, the opposite is true (For interpretation of the references to color in this figure legend, the reader is referred to the web version of this article).
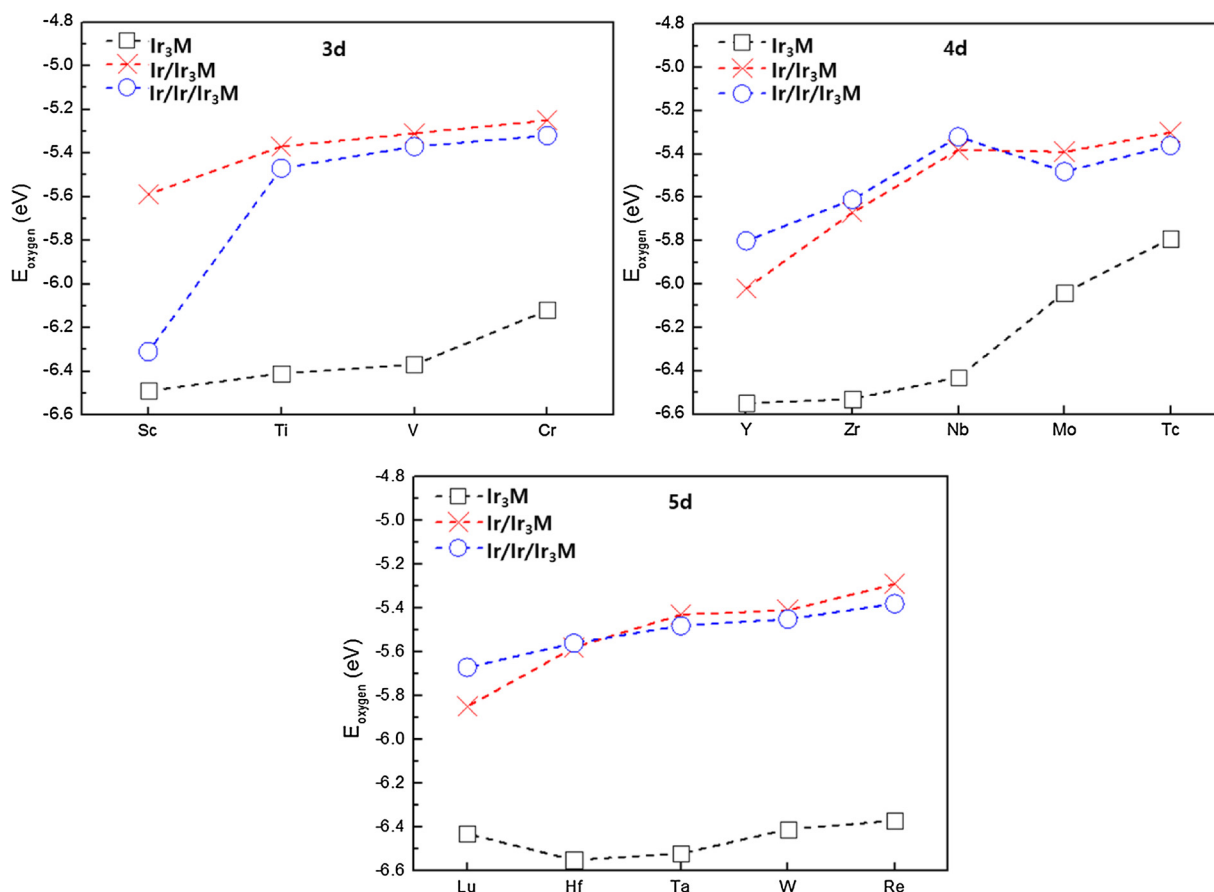
Fig. 3. The calculated oxygen adsorption energies at the surface of Ir$_3$M(111), Ir/Ir$_3$M(111), and Ir/Ir/Ir$_3$M(111) slabs are shown in square, cross, and circle respectively, where M exhibits 3 d (top left), 4 d (top right), and 5 d (bottom) metals.

oxygen adsorption energy [E$_{b,O}$] for all surface models [E$_{b,O}$(Ir$_3$Sc) = −6.49 eV, E$_{b,O}$(Ir$_3$Ti) = −6.41 eV, E$_{b,O}$(Ir$_3$V) = −6.37 eV, E$_{b,O}$(Ir$_3$Cr) = −6.12 eV, E$_{b,O}$(Ir$_3$Y) = −6.55 eV, E$_{b,O}$(Ir$_3$Zr) = −6.53 eV, E$_{b,O}$(Ir$_3$Nb) = −6.41 eV, E$_{b,O}$(Ir$_3$Mo) = −6.04 eV, E$_{b,O}$(Ir$_3$Tc) = −5.79 eV, E$_{b,O}$(Ir$_3$Lu) = −6.43 eV, E$_{b,O}$(Ir$_3$Hf) = −6.55 eV, E$_{b,O}$(Ir$_3$Ta) = −6.52 eV, E$_{b,O}$(Ir$_3$W) = −6.91 eV, E$_{b,O}$(Ir$_3$Zr) = −5.87 eV] than the pure Ir(111) case [E$_{b,O}$ = 5.37 eV], implying the increased affinity for oxygen and in turn reduction of ORR activity in Ir$_3$M/Ir$_3$M(111) compared to the pure Ir(111) surface.

On the other hand, for the Ir-*skinlayer* (monolayer or bilayer) cases, the affinity for oxygen is greatly decreased compared to the Ir$_3$M/Ir$_3$M (111) case. In particular, the weakening of O–Ir bond strength is the highest in the Ir/Ir$_3$V(111), Ir/Ir$_3$Cr(111), Ir/Ir$_3$Tc(111), Ir/Ir$_3$Re(111) (Ir monolayer) and Ir/Ir/Ir$_3$Nb(111) (Ir bilayer case) cases [here, the most favorable adsorption site is the fcc hollow site, except for Ir$_3$W and Ir$_3$Re (where the oxygen is adsorbed at the top site)], leading to the noticeably decreased affinity for oxygen compared to the pure Ir(111) case and possibly enhancement of the catalytic activity toward ORR. Note that the E$_{ad,O}$ of Ir-*skinlayer* cases is increased by 0.06 eV(Ir/Ir$_3$V), 0.15 eV(Ir/Ir$_3$Cr), 0.07 eV(Ir/Ir$_3$Tc), 0.08 eV (Ir/Ir$_3$Re) and 0.05 eV(Ir/ Ir/Ir$_3$Nb) in comparison with the pure Ir(111) surface. The decrease in E$_{ad,O}$ is possibly due to the Ir surface being geometrically and electronically modified by the subsurface Ir$_3$M (this will be analyzed in-depth in later section).

Overall, through the calculation of oxygen adsorption energy, we were able to reveal possible candidates for better ORR catalytic activity than pure Ir(111) surface, and the candidates are V, Cr, Tc, and Re of Ir/ Ir$_3$M(111), and Cr, Nb and Tc of Ir/Ir/Ir$_3$M(111). More importantly, we discovered that the Ir-skinlayers play important role of reducing the

oxygen binding energy when compared to the bulk-terminated Ir$_3$M (111) case.

3.3. Stability of Ir skinlayer in Ir$_3$M alloy catalysts

According to the previous studies, the surface structures of bimetallic catalysts change upon gas adsorption due to the metal segregation on surface [1,23,28]. At elevated temperatures, Ir$_3$M alloy catalysts undergo the surface segregation, which lead to the formation of the pure Ir layers(skinlayer) or the enrichment of M components at the surface layer on the top of Ir$_3$M catalysts that substantially decreases or increases the oxygen affinity of catalytic surfaces and in turn affects ORR catalysis [1,23,28].

In order to further demonstrate the stability of the promising candidates for improving ORR activity [which are V, Cr, Tc, Re of Ir/Ir$_3$M (111), and Cr, Nb, Tc of Ir/Ir/Ir$_3$M(111)], we first calculated the segregation energy of core M element toward surface layer in the Ir-skinlayer catalysts at clean(bare) (indicated by ΔE_{seg}^{clean}) and oxygen (indicated by ΔE_{seg}^{oxygen}) environment, which are defined by the following equation;

$$\Delta E_{seg}^{clean} = E_F^{clean} - E_i^{clean} \qquad (5)$$

$$\Delta E_{seg}^{oxygen} = E_F^{oxygen} - E_i^{oxygen} \qquad (6)$$

where E$_F^{clean}$ (or E$_F^{oxygen}$) is the total energy of the Ir-skinlayer supported on the bare (or oxygen-adsorbed) Ir$_3$M(111) slab where the segregation of core M element toward the surface layer is occurred and E$_i^{clean}$ (or E$_i^{oxygen}$) is the initial reference energy where no M segregation is proceeded (See Supporting information Fig. S1 for the visualized surface
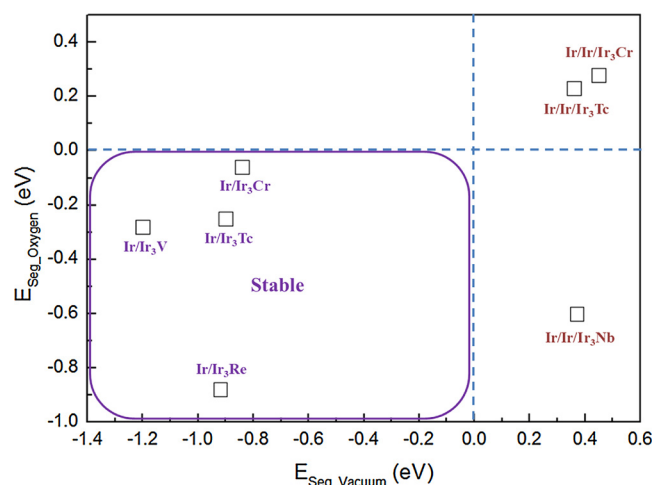
Fig. 4. The calculated segregation energies of the selected Ir₃M(111), Ir/Ir₃M (111), and Ir/Ir/Ir₃M(111) slabs are displayed. X-axis and Y-axis represent the segregation energy under vacuum and oxygen environment, respectively.

Fig. 5. The oxygen adsorption energy (indicated by circle symbol) for the screened four Ir/Ir₃M (111) (M = Cr, V, Tc, Re) catalysts as a function of the change in the lattice parameter with respect to pure Ir(111) case. Here, the contribution of the pure strain effect to the total oxygen binding energy on four different strained Ir(111) surfaces [whose lattice parameters are corresponding to that of four Ir₃M(M = Cr, V, Tc, Re) catalysts] is shown in square symbol and vertical orange arrow. The contribution of the pure ligand effect to the total oxygen binding energy (denoted as the vertical blue arrow) can be determined by subtracting the strain contribution from the total oxygen binding energy (For interpretation of the references to color in this figure legend, the reader is referred to the web version of this article).

segregation process). Here, the positive (endothermic) ΔE_{seg}^{vacuum} and ΔE_{seg}^{oxygen} value indicates that the Ir-skinlayer of Ir₃M(111) catalyst is unlikely to undergo surface segregation, while for the negative(exothermic) segregation value the opposite is true [32].

As shown in Fig. 4, the ΔE_{seg}^{clean} (or ΔE_{seg}^{oxygen}) for the Ir monolayer of Ir₃V(111), Ir₃Cr(111), Ir₃Tc(111) and Ir₃Re(111) is calculated to be exothermic by 1.20 eV (0.28 eV), 0.84 eV(0.06 eV), 0.90 eV(0.25 eV) and 0.92 eV(0.88 eV) at both clean and oxygen conditions, indicating that the Ir monolayer catalyst of Ir₃V(111), Ir₃Cr(111), Ir₃Tc(111) and Ir₃Re(111) can be stable at ORR condition, together with the enhanced ORR activity.

In contrast, for the Ir bilayer catalysts (Cr, Nb, Tc cases), none of candidates satisfy the condition where both ΔE_{seg}^{clean} and ΔE_{seg}^{oxygen} > 0 eV, suggesting that there exists the high chance that the Ir bilayer supported on Ir₃M(111) would undergo the surface segregation where the M element from the subsurface layer migrates to the top surface layer.

3.4. Underlying mechanism of Ir/Ir₃M toward enhanced ORR activity

Our goal is to rationally design the Ir₃M alloy catalysts with enhanced ORR activity and high stability, and thus three criteria should be met simultaneously. That is, the exothermic formation energy of bulk Ir₃M alloy and endothermic segregation energy of core M element toward surface layer at both clean and oxygen environment. Throughout these calculation procedures, we have successfully narrowed down to four possible Ir₃M catalysts with better ORR activity and stability. That is, the Ir/Ir₃M(111) surface models where M is Cr, V, Tc, and Re.

To better understand the role of Ir-skinlayer in enhancing catalytic activity, we scrutinized how the alloying effects implanted in the Ir₃M alloy catalysts affect the adsorption energy. Here, two alloying mechanisms play important role in a modification in the ORR catalytic activity of the Ir/Ir₃M(111) surface. One is the mismatch of lattice parameters (refer to lp) between alloying Ir and M components (so-called strain effect), and the second is the interaction of d orbitals between surface Ir and subsurface M atoms [the so-called electronic (ligand) effect] [33–36].

To elucidate the relative role of each alloying effect, we first decoupled the strain effect from the electronic (ligand) effect in the Ir/Ir₃M(111) catalyst by calculating the oxygen binding energy [defined as $E_{b,O}^{strained}$, which represents the contribution of the pure strain effect to the total oxygen binding energy] on four different strained Ir(111) surfaces [indicated by Ir₍ₗₚ₎(111)] whose lattice parameters (lp) are
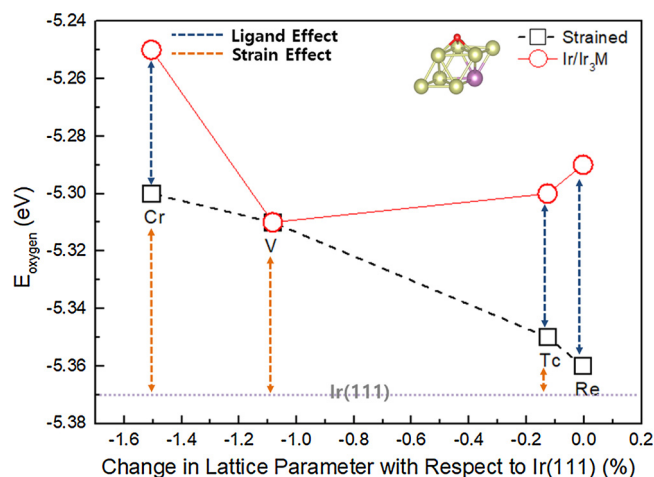
corresponding to that of four Ir₃M candidates [34,35].

According to our DFT calculation, the Ir monolayer of four Ir₃Re, Ir₃Tc, Ir₃V, and Ir₃Cr candidates is under compressively strained environment. Note that the surface lattice distance of Ir₃Re, Ir₃Tc, Ir₃V, and Ir₃Cr is predicted to be reduced to 3.8813 Å, 3.8765 Å, 3.8394 Å, and 3.8230 Å, respectively, compared to the pure Ir(111) surface (3.8814 Å).

Fig. 5 depicts the variation of the $E_{b,O}^{strained}$ on the strained Ir₃.₈₈₁₃(111) (for Re), Ir₃.₈₇₆₅(111) (for Tc), Ir₃.₈₃₉₄(111) (for V) and Ir₃.₈₂₃₀(111) (for Cr) surfaces (see the dotted black line). We find that the $E_{b,O}^{strained}$ tends to be reduced by the increase of the level of lattice contraction (the higher the surface lattice contraction is, the weaker the O−Ir bond strength is). In particular, the Ir₃.₈₂₃₀(111) slab (whose compressively strained environment is imposed by alloying Ir with Cr) exhibits the highest increase of oxygen binding energy ($E_{b,O}^{strained}$ = −5.30 eV) among four candidates, leading to the reduced oxygen affinity by 0.07 eV compared to the pure Ir(111) case.

To clearly understand the above-mentioned relationship between strain and activity, we calculate d band centers from the plot of the local density of states (LDOS) projected onto the d states of surface Ir atoms for the strained Ir(111) surfaces (see Fig. 6 and Supporting information Table S3). We find that the d band centers strongly depend on the imposed compressive strain. In particular, the higher amount of the compressive strain leads to the larger downshift of the d-band center and in turn the higher increase of oxygen binding energy (decrease of oxygen affinity). For example, as the level of compressive surface strain increases from −0.003% (Ir₃Re) to −0.127% (Ir₃Tc) to −1.083% (Ir₃V) to −1.505% (Ir₃Cr) with respect to the pure Ir(111) case, the d band centers correspondingly move down from −1.84 eV to −1.86 eV to −1.90 eV to −1.92 eV and this downshift of d band centers in comparison to pure Ir (−1.84 eV) reduced $E_{b,O}^{strained}$ by 0.017 eV, 0.024 eV, 0.058 eV, and 0.071 eV for Re, Tc, V, and Cr, respectively. Our calculation of strain effect in the modification of surface activity is in a good agreement with the previous studies where an upshift(downshift) of the d band center in a catalyst leads to a stronger (weaker) interaction with an adsorbate [33,34].

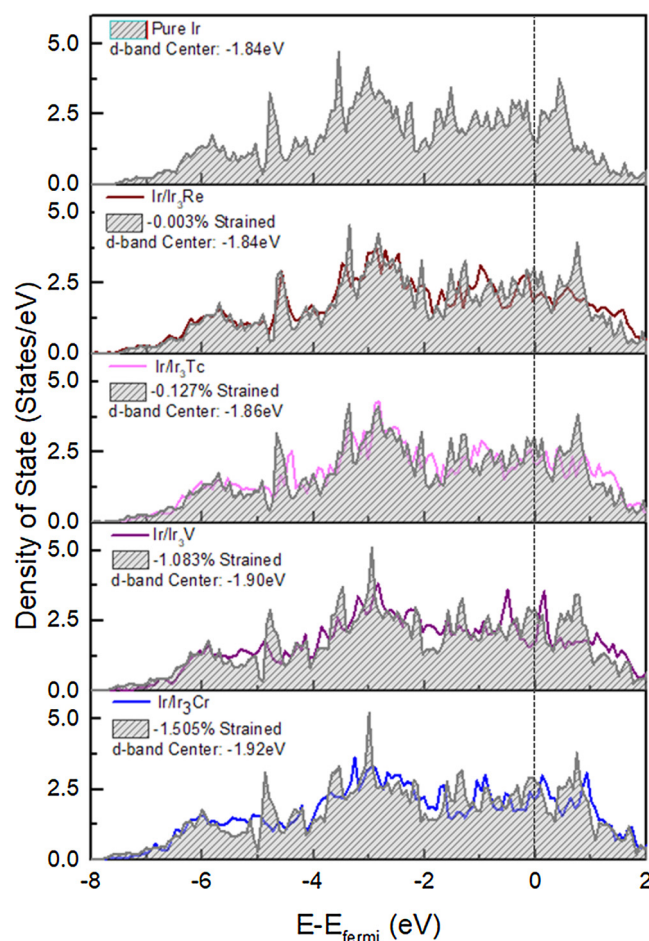We further examined the contribution of the pure ligand effect to

Fig. 6. From the top, the plots of the local density of states (LDOS) projected on the d states of surface Ir atoms for pure Ir(111), Ir/Ir₃Re (111), Ir/Ir₃Tc (111), Ir/Ir₃V (111), and Ir/Ir₃Cr (111) cases are displayed in solid colored lines. The grey filled plot represents the LDOS for the strained Ir(111) surfaces, which are caused by the equilibrium lattice constant of Ir₃M (M = Re, Tc, V, Cr) alloy (the amount of strain imposed on surface is shown in the top left side). The calculated d band center is also shown in Figure. The displayed dashed line at 0 eV represents the fermi level position.

Fig. 7. The contribution of the pure ligand effect to the total oxygen binding energy ($\Delta E_{b,O}^{ligand}$) in Ir/Ir₃M system as a function of the percentage of unoccupied d states (which is deviated from the unoccupancy of pure Ir case).

between surface Ir atoms and subsurface M atoms in Ir/Ir₃M(111) catalyst. Table S3 shows the charge distribution of Ir/Ir₃M(111) model slab predicted by Bader charge analysis [37]. We find that the Ir/Ir₃Re (111) exhibits the highest increase of charge density at the surface layer ($\Delta\sigma = 0.486e$), followed by Ir/Ir₃Cr(111) ($\Delta\sigma = 0.324e$), Ir/Ir₃Tc(111) ($\Delta\sigma = 0.454e$) and Ir/Ir₃Re(111) ($\Delta\sigma = 0.004e$), which is corresponding to the order of the ligand contribution.

3.5. Electrochemical performance of Ir₃Cr skin alloy

Fig. 8a shows X-ray Diffraction (XRD) patterns of Ir/Ir₃Cr/C electrocatalyst, synthesized by physical vapor deposition method (PVD). In diffraction patterns of Ir/Ir₃Cr/C, the peaks of 41.1°, 47.8°, 69.9° and 84.5° corresponds to the (111), (200), (220), and (311) planes respectively, which is consistent with standard diffraction patterns of pure Ir₃Cr (PDF #65-1811, vertical red line). Even though small peaks around 38.8° and 43° corresponding to Ir₁Cr₁ (PDF #65-7001) are observed, the intensity is relatively negligible compared to that of the Ir₃Cr peaks. These results indicate that the most of IrCr alloy NPs, synthesized by PVD method, have a Ir₃Cr phase. In addition, by comparing with the XRD patterns of Ir/C (Fig. S3), peak shift toward a higher angle. Specifically, the main peaks of Ir and Ir/Ir₃Cr are 40.67° and 41.11° respectively, and the lattice parameters calculated by Bragg eq. decreased from 2.21 Å to 2.19 Å by about 1.03%. XRD provides data, based on the bulk structure of the catalyst, not the surface, which makes it difficult to determine the exact strain value of the surface of catalysts. Therefore, the numerical difference between the calculation and the experimental results is indispensable. Nevertheless, XRD analysis shows a similar conclusion to the calculation results that compressive strain is generated by the alloy of Ir and Cr. To ensure the elemental composition, Energy-dispersive X-ray spectroscopy (EDS) analysis of IrCr/C was performed and the results are shown in Fig. 8b. The atomic ratio of Ir to Cr of the prepared IrCr/C was 3.17, which was not only consistent with the XRD results, but it also indicates that the prepared IrCr/C was synthesized as originally intended. The Transmission electron microscopy (TEM) image (Fig. 8c) shows that IrCr nanoparticles of about 3 nm in size are evenly dispersed on carbon support. As shown in TEM images of Ir/C (Fig. S4), the size of Ir NPs was found to be in the range of 1 to 2 nm which is smaller than Ir/Ir₃Cr NPs. The increase in the size of the Ir/Ir₃Cr NPs may have been caused by the agglomeration of NPs during the high temperature treatment (750 °C) of the synthesis process. We also map the distribution of Ir and Cr elements through STEM-EDS analysis. The Scanning transmission electron microscopy (STEM) image and the corresponding EDS

the total oxygen binding energy (indicated by $E_{b,O}^{ligand}$), which is obtained by subtracting the $E_{b,O}^{strained}$ of Ir strained surfaces from the $E_{b,O}$ of Ir/Ir₃M (111) catalyst [$E_{b,O}^{ligand} = E_{b,O} - E_{b,O}^{strained}$] [33,35]. We find the positive value of $E_{b,O}^{ligand}$ for all Ir/Ir₃M(111) catalysts, suggesting that the ligand contribution is in the same direction as compressive strain contribution, leading to the further increase of binding energy (decrease of oxygen affinity). Notice that the order of the ligand contribution is Ir/Ir₃Re (111) [$E_{b,O}^{ligand} = 0.062$ eV] > Ir/Ir₃Cr(111) [$E_{b,O}^{ligand} = 0.053$ eV] > Ir/Ir₃Tc(111) [$E_{b,O}^{ligand} = 0.046$ eV] > Ir/Ir₃V(111) [$E_{b,O}^{ligand} = 0.004$ eV].

The different ligand contribution can be better understood by the change of the number of unoccupied d states above the Fermi level (which is defined as d-band unoccupancy) for the surface Ir atoms in Ir₃M catalysts. Fig. 7 exhibits the variation of oxygen binding energy ($E_{b,O}^{ligand}$) in Ir/Ir₃M as a function of the number of unoccupied d states (see the Fig. S5 of Supporting information for strain-free LDOS). We find the increase of ligand contribution [0.062 eV (Ir/Ir₃Re), 0.053 eV (Ir/Ir₃Cr), 0.046 eV (Ir/Ir₃Tc) and 0.004 eV (Ir/Ir₃V)] by the decrease of d-band unoccupancy [–1.04% (Ir/Ir₃Re), –0.70% (Ir/Ir₃Cr), –0.29% (Ir/Ir₃Tc) and –0.19% (Ir/Ir₃V)], suggesting that the reduction in the density of unoccupied d states for the surface Ir atoms may be a key factor in increasing the ligand contribution to the total oxygen adsorption energy. The variation of d-band unoccupancy is related to the surface charge polarization induced by the electronic charge transfer
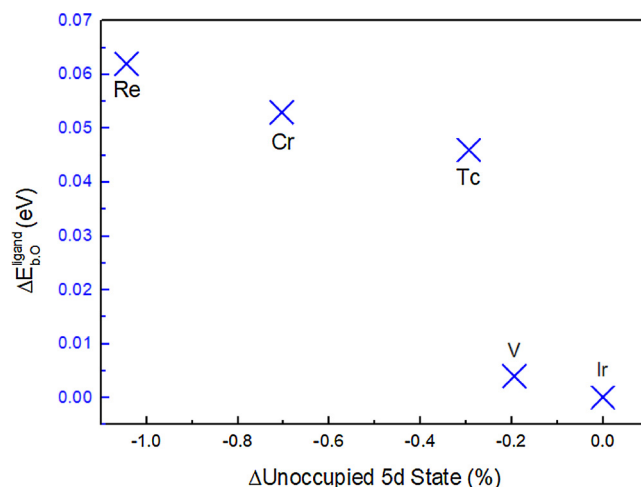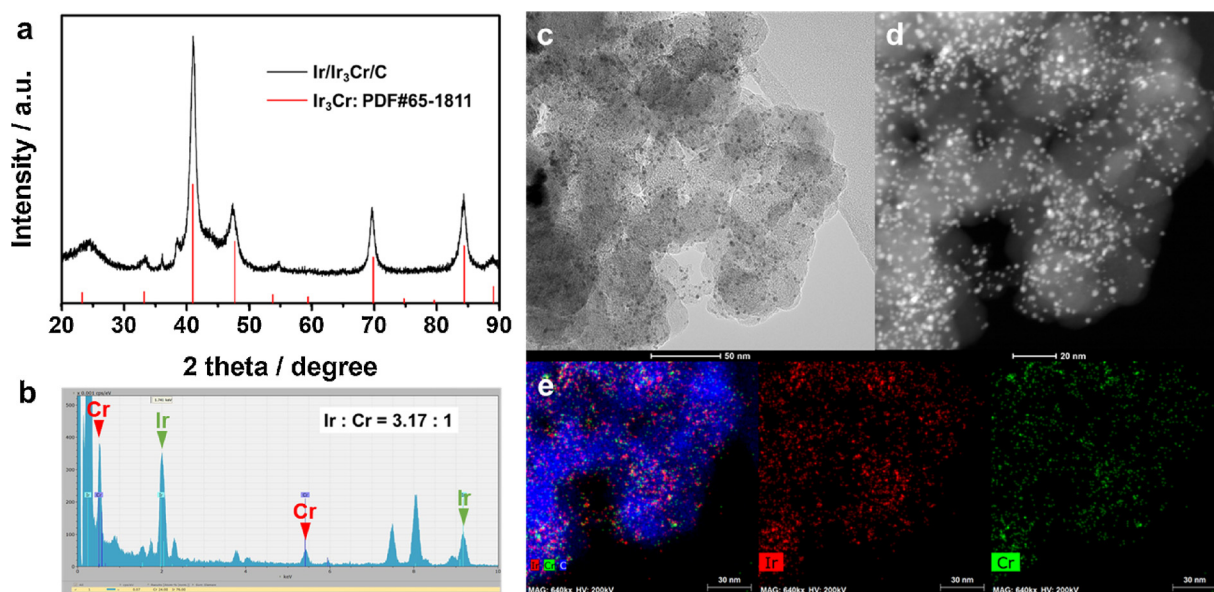
Fig. 8. Physical characteristics (a) X-ray diffraction (XRD) pattern of Ir/Ir₃Cr alloy NCs. Positions of standard diffraction peaks of Ir₃Cr (PDF #65-1811) are marked by the vertical red lines. (b) Transmission electron microscopy (TEM) energy dispersive X-ray spectroscopy (EDS) analysis of Ir/Ir₃Cr/C. (c) TEM image of Ir/Ir₃Cr/C. (d, e) High-angle annular dark field (HAADF) image and corresponding elemental mappings (Ir, Cr, and C) of Ir/Ir₃Cr/C (For interpretation of the references to color in this figure legend, the reader is referred to the web version of this article).

elemental maps of Ir/Ir₃Cr are shown in Fig. 8d and e. The Ir and Cr EDS analysis demonstrated a homogeneous distribution of each element across the IrCr particles.

In order to confirm the formation of Ir-rich shell on the surface of Ir/Ir₃Cr nanoparticles, EDS-line profiling analysis was applied. As shown in Fig. 9a, the Ir and Cr composition distributions are observed in a single nanoparticle. A line scan was performed across the center of the about 10 nm circular particle. The highest intensity is observed in the middle of the particle and gradually decrease toward the end of the particles, which demonstrate that the particle has a spherical shape (Fig. 9b). In particular, as shown in Fig. 9c, the profile of Cr ratio was semicircular, whereas the that of Ir ratio was U-shaped. Therefore, the ratio of Ir element on the surface of the particle is higher than the center, which demonstrates that the Ir-rich shell is formed on the top of Ir/Ir₃Cr nanoparticles. Here, we performed the energy dispersive X-ray spectroscopy (EDS) analysis using a FEI Talos™ TEM (Fig. S7) and then the area of the elemental distributions were determined using ImageJ program with an auto threshold (Huang) process and circular equivalent radius of elemental distributions were determined to investigate the thickness of Ir layers in Ir/Ir₃Cr [38–40]. Given that the thickness of pure Ir is about 0.21 nm (Fig. S8) and the average thickness of Ir shell is 0.18 nm in Ir/Ir₃Cr, it can be concluded that the depth of Ir skin layer is monolayer.

The electro-chemical experiment was performed to investigate the improvement of ORR activity by alloying Ir by Cr. ORR polarization curves for Ir/C and Ir/Ir₃Cr/C catalysts was shown in Fig. 10a. For both catalysts, the curves consisted of two distinct potential regions. One is a diffusion-limiting region formed between 0.1 V and 0.4 V, and the other is a kinetic-diffusion control region between 0.4 V and 0.8 V, which is typical ORR polarization curve. Fig. 10a shows that the activity for ORR is improved on the Ir/Ir₃Cr/C compared to Ir/C resulting in a positive shift of 113 mV at half-wave potential. As discussed above, the difference in the size of Ir and Ir₃Cr actually causes a difference in the area that can participate in the oxygen reduction reaction. That is, the smaller the size of the particles, the greater the area is exposed to the surface, which is advantageous for the electro-chemical reaction. As might be expected, the smaller size of the Ir NPs would have contributed to the formation of larger ECSA than that of Ir/Ir₃Cr (Fig. S5). Therefore, eliminating the ORR activity change caused by the difference in electro-chemical active surface area (ECSA), the specific activity is noteworthy in that it can compare the intrinsic characteristics toward ORR of the catalysts by normalizing ORR kinetic current with ECSA. Fig. 10b compares the specific activities of Ir/C and Ir/Ir₃Cr/C based on ECSA calculated from H_{upd}. The specific activity (at 0.7 V vs RHE) of Ir/Ir₃Cr/C (1.180 mA cm⁻²) was 12.3 times higher than Ir/C (0.096 mA cm⁻²).
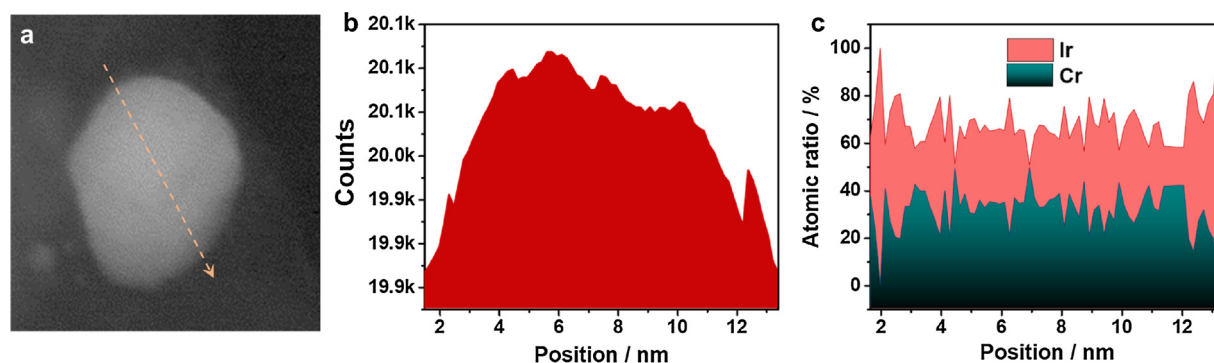

Fig. 9. Microscopic and compositional observations of a single Ir/Ir₃Cr nanoparticle electrocatalyst. (a) HAADF image of single Ir/Ir₃Cr NP, (b) Intensity and (c) Distribution of components in the Ir/Ir₃Cr nanoparticle obtained by the line-scan analysis using TEM-EDS.
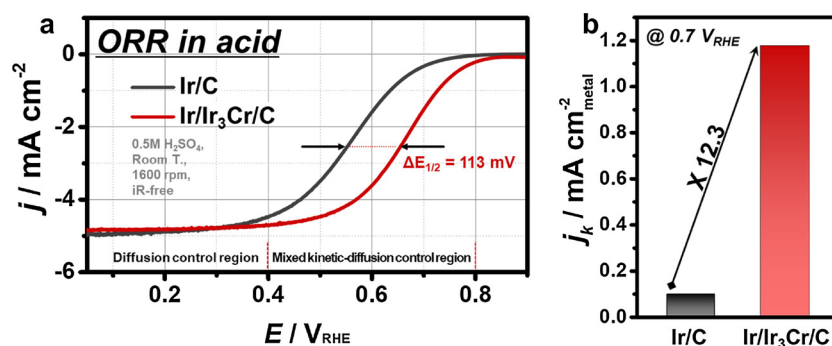
Fig. 10. Evaluation of oxygen reduction reaction activity (a) Ohmic resistance-compensated polarization curves for ORR (b) Calculated specific activities of Ir/C and Ir/Ir$_3$Cr/C.
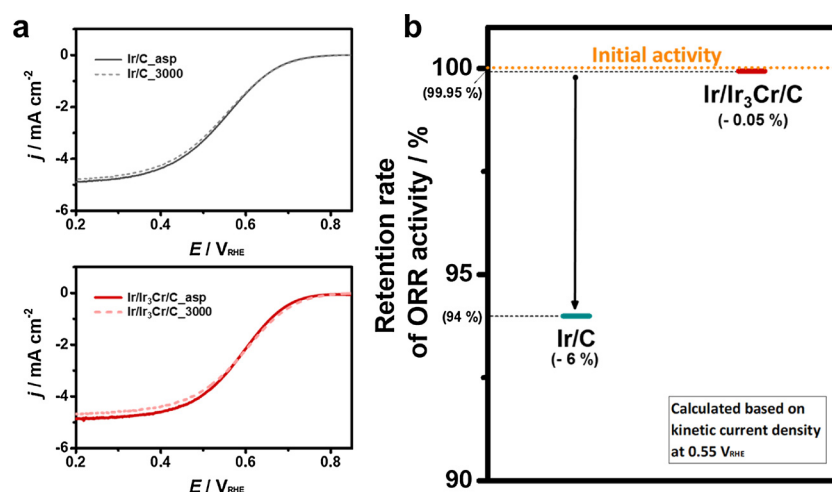

Fig. 11. Evaluation of electro-chemical durability (a) ORR polarization curves of Ir/C catalyst and Ir/Ir$_3$Cr/C catalyst before, and after 3000 potential cycles between 0.6 and 1.0 V (vs. RHE). (b) The retention rate of kinetic current density (at 0.55 V vs. RHE) after 3000 potential cycles.

We evaluated the electro-chemical durability of the Ir/Ir$_3$Cr/C catalyst through consecutive cyclic voltammetry between 0.6 V and 1.0 V (vs RHE, 3000 cycles) in Ar-saturated 0.5 M H$_2$SO$_4$ with a scan rate of 50 mV/s at room temperature. For comparison, the electrochemical durability evaluation of Ir/C was also performed under the same conditions as Ir/Ir$_3$Cr/C. After 3000 potential cycles, the Ir/Ir$_3$Cr/C catalyst maintained its initial activity throughout the entire potential range. On the other hand, the Ir/C catalyst is relatively unstable under the same durability test conditions. The polarization curve shows a slightly negative shift after 3000 potential cycles (Fig. 11a). The kinetic current density (at 0.55 V vs. RHE) of Ir/Ir$_3$Cr/C before and after durability test were 9.515 and 9.511 mA/cm^2, respectively, showing only 0.05% decrease from the initial activity. This result demonstrates an improved electro-chemical durability of Ir/Ir$_3$Cr/C catalyst by comparing with the ORR activity change of Ir/C which shows about 6% decrease from initial ORR activity under the same conditions (Fig. 11b). In addition to the improvement of activity of Ir/Ir$_3$Cr, the improvement of durability is also in a good agreement with the computational calculation results.

4. Conclusion

In this study, we systematically designed the novel Ir-based ORR catalyst for the PEMFC application via the combined DFT and experimental approach.

First, we computationally screened the potential M element and near-surface composition in Ir$_3$M nanoalloy (M = 3 d, 4 d, 5 d metals) for the purpose of enhancing the activity and durability of catalyst in ORR. Here, the criteria for finding such promising candidate is (i) the thermodynamic stability of Ir$_3$M toward alloy formation [represented by Gibbs free energy change for alloy formation process], (ii) the activity of Ir$_3$M toward ORR [indicated by oxygen binding energy], and (iii) the durability of Ir$_3$M under ORR condition [denoted as segregation energy of inside M element toward surface layer under vacuum and oxygen environment]. Our DFT-based screening identified the pure Ir monolayer on the top of Ir$_3$Cr, Ir$_3$V, Ir$_3$Re, and Ir$_3$Tc alloy cores as the promising candidates for improving ORR activity and durability.

Second, we prepared a pure Ir monolayer catalyst (so-called Ir skinlayer) on the top of Ir$_3$Cr core (the Cr element case may display the most improved ORR activity among the computationally-searched candidates) by means of physical vapor deposition (PVD) for justifying our DFT prediction. We successfully synthesized a 3 nm Ir-covered (Ir skinlayer) Ir$_3$Cr nanoparticle whose surface lattice distance was contracted by 1.03% compared to the pure Ir case. This was confirmed by the XRD and TEM-EDS analysis. The evaluation of ORR activity was performed at 0.7 V vs RHE and the activity of Ir skinlayer/Ir$_3$Cr catalyst (1.180 mA cm^{-2}) indicated the 12.3 times higher than the pure Ir case (0.096 mA cm^{-2}). The stability of Ir skinlayer/Ir$_3$Cr catalyst at ORR condition was in a good agreement with our DFT result; That is, the kinetic current density of a Ir skinlayer/Ir$_3$Cr catalyst at 0.55 V vs. RHE after 3000 cycles depicted only 0.05% decrease from the initial activity, whereas for the Ir case the reduction of current density by 6% was detected.

Finally, the fundamental mechanism of such enhanced ORR activity in the pure Ir monolayer on the top of Ir$_3$Cr, Ir$_3$V, Ir$_3$Re, and Ir$_3$Tc alloy cores was further examined by unraveling the relative role of each alloying effect [so-called strain and electronic (ligand) effects] to the total oxygen affinity. Our DFT calculation suggested that the variation in the number of unoccupied d states and lattice distance of the surface Ir

atoms play an important role in reducing oxygen affinity and in turn enhancing ORR activity. In particular, the lattice contraction (leading to the down-shift of d-band) and electronic charge gain (resulting in the decrease of d-band unoccupancy) of the surface Ir atoms is responsible for reducing oxygen affinity of Ir_3M (M = Cr, Re, Tc and V) catalyst.

Our theoretical and experimental study highlight the general methodology for designing metal-based alloy catalysts for the application to ORR in PEMFC and such method can be further extended to the development of the next-level electrocatalyst for energy conversion.

Appendix A. Supplementary data

Supplementary material related to this article can be found, in the online version, at doi:https://doi.org/10.1016/j.apcatb.2018.04.077.

References

[1] L. Ou, Design of pd-based bimetallic catalysts for ORR: a DFT calculation study, J. Chem. (2015) 11 2015.

[2] S.C. Tjong, Polymer nanocomposite bipolar plates reinforced with carbon nanotubes and graphite nanosheets, Energy Environ. Sci. 4 (3) (2011) 605–626.

[3] M.H. Shao, Q.W. Chang, J.P. Dodelet, R. Chenitz, Recent advances in electrocatalysts for oxygen reduction reaction, Chem. Rev. 116 (6) (2016) 3594–3657.

[4] K.S. Lee, H.Y. Park, H.C. Ham, S.J. Yoo, H.J. Kim, E. Cho, A. Manthiram, J.H. Jang, Reversible surface segregation of Pt in a Pt3Au/C catalyst and its effect on the oxygen reduction reaction, J. Phys. Chem. C 117 (18) (2013) 9164–9170.

[5] C.E. Kim, D.H. Lim, J.H. Jang, H.J. Kim, S.P. Yoon, J. Han, S.W. Nam, S.A. Hong, A. Soon, H.C. Ham, Effect of gold subsurface layer on the surface activity and segregation in Pt/Au/Pt3M (where M=3d transition metals) alloy catalyst from first-principles, J. Chem. Phys. 142 (3) (2015).

[6] J.L. Fernandez, V. Raghuveer, A. Manthiram, A.J. Bard, Pd-Ti and Pd-Co-Au electrocatalysts as a replacement for platinum for oxygen reduction in proton exchange membrane fuel cells, J. Am. Chem. Soc. 127 (38) (2005) 13100–13101.

[7] G.M. Jiang, H.Y. Zhu, X. Zhang, B. Shen, L.H. Wu, S. Zhang, G. Lu, Z.B. Wu, S.H. Sun, Core/shell face-centered tetragonal FePd/Pd nanoparticles as an efficient non-Pt catalyst for the oxygen reduction reaction, ACS Nano 9 (11) (2015) 11014–11022.

[8] M. Wang, W.M. Zhang, J.Z. Wang, D. Wexler, S.D. Poynton, R.C.T. Slade, H.K. Liu, B. Winther-Jensen, R. Kerr, D.Q. Shi, J. Chen, PdNi hollow nanoparticles for improved electrocatalytic oxygen reduction in alkaline environments, ACS Appl. Mater. Interfaces 5 (23) (2013) 12708–12715.

[9] D.A. Slanac, W.G. Hardin, K.P. Johnston, K.J. Stevenson, Atomic ensemble and electronic effects in Ag-rich AgPd nanoalloy catalysts for oxygen reduction in alkaline media, J. Am. Chem. Soc. 134 (23) (2012) 9812–9819.

[10] A. Holewinski, J.C. Idrobo, S. Linic, High-performance Ag-Co alloy catalysts for electrochemical oxygen reduction, Nat. Chem. 6 (9) (2014) 828–834.

[11] J.X. Wang, H. Inada, L.J. Wu, Y.M. Zhu, Y.M. Choi, P. Liu, W.P. Zhou, R.R. Adzic, Oxygen reduction on well-defined core-shell nanocatalysts: particle size, facet, and Pt Shell thickness effects, J. Am. Chem. Soc. 131 (47) (2009) 17298–17302.

[12] Y.G. Suo, L. Zhuang, J.T. Lu, First-principles considerations in the design of Pd-alloy catalysts for oxygen reduction, Angew. Chem. Int. Ed. 46 (16) (2007) 2862–2864.

[13] P. Strasser, S. Koh, T. Anniyev, J. Greeley, K. More, C.F. Yu, Z.C. Liu, S. Kaya, D. Nordlund, H. Ogasawara, M.F. Toney, A. Nilsson, Lattice-strain control of the activity in dealloyed core-shell fuel cell catalysts, Nat. Chem. 2 (6) (2010) 454–460.

[14] J. Greeley, J.K. Norskov, Combinatorial density functional theory-based screening of surface alloys for the oxygen reduction reaction, J. Phys. Chem. C 113 (12) (2009) 4932–4939.

[15] S.J. Guo, S. Zhang, S.H. Sun, Tuning nanoparticle catalysis for the oxygen reduction reaction, Angew. Chem. Int. Ed. 52 (33) (2013) 8526–8544.

[16] J.W.F. To, J.W.D. Ng, S. Siahrostami, A.L. Koh, Y. Lee, Z. Chen, K.D. Fong, S. Chen, J. He, W.-G. Bae, J. Wilcox, H.Y. Jeong, K. Kim, F. Studt, J.K. Nørskov, T.F. Jaramillo, Z. Bao, High-performance oxygen reduction and evolution carbon catalysis: from mechanistic studies to device integration, Nano Res. 10 (4) (2017) 1163–1177.

[17] G.E. Ramirez-Caballero, Y. Ma, R. Callejas-Tovar, P.B. Balbuena, Surface segregation and stability of core-shell alloy catalysts for oxygen reduction in acid medium, Phys. Chem. Chem. Phys. 12 (9) (2010) 2209–2218.

[18] E. Antolini, Iridium as catalyst and cocatalyst for oxygen evolution/reduction in acidic polymer electrolyte membrane electrolyzers and fuel cells, ACS Catal. 4 (5) (2014) 1426–1440.

[19] S.C. Perry, G. Denuault, The oxygen reduction reaction (ORR) on reduced metals: evidence for a unique relationship between the coverage of adsorbed oxygen species and adsorption energy, Phys. Chem. Chem. Phys. 18 (15) (2016) 10218–10223.

[20] D.E. Ramaker, A. Korovina, V. Croze, J. Melke, C. Roth, Following ORR intermediates adsorbed on a Pt cathode catalyst during break-in of a PEM fuel cell by in operando x-ray absorption spectroscopy, Phys. Chem. Chem. Phys. 16 (27) (2014) 13645–13653.

[21] D. Yang, B. Li, H. Zhang, J. Ma, Kinetics and electrocatalytic activity of IrCo/C catalysts for oxygen reduction reaction in PEMFC, Int. J. Hydrog. Energy 37 (3) (2012) 2447–2454.

[22] D. Cheng, X. Qiu, H. Yu, Enhancing oxygen reduction reaction activity of Pt-shelled catalysts via subsurface alloying, Phys. Chem. Chem. Phys. 16 (38) (2014) 20377–20381.

[23] L. Ou, S. Chen, Comparative study of oxygen reduction reaction mechanisms on the Pd(111) and Pt(111) surfaces in acid medium by DFT, J. Phys. Chem. C 117 (3) (2013) 1342–1349.

[24] G. Kresse, M. Marsman, J. Furthmüller, VASP The Guide, Vienna University of Technology, 2001.

[25] J.P. Perdew, K. Burke, M. Ernzerhof, Generalized gradient approximation made simple, Phys. Rev. Lett. 77 (18) (1996) 3865–3868.

[26] P.E. Blöchl, J. Kästner, C.J. Först, Electronic structure methods: augmented waves, pseudopotentials and the projector augmented wave method, in: S. Yip (Ed.), Handbook of Materials Modeling: Methods, Springer, Netherlands: Dordrecht, 2005, pp. 93–119.

[27] J. Greeley, I.E. Stephens, A.S. Bondarenko, T.P. Johansson, H.A. Hansen, T.F. Jaramillo, J. Rossmeisl, I. Chorkendorff, J.K. Norskov, Alloys of platinum and early transition metals as oxygen reduction electrocatalysts, Nat. Chem. 1 (7) (2009) 552–556.

[28] H.-C. Tsai, Y.-C. Hsieh, T.H. Yu, Y.-J. Lee, Y.-H. Wu, B.V. Merinov, P.-W. Wu, S.-Y. Chen, R.R. Adzic, W.A. Goddard, DFT study of oxygen reduction reaction on Os/Pt core–shell catalysts validated by electrochemical experiment, ACS Catal. 5 (3) (2015) 1568–1580.

[29] D.-H. Lim, J. Wilcox, Mechanisms of the oxygen reduction reaction on defective graphene-supported Pt nanoparticles from first-principles, J. Phys. Chem. C 116 (5) (2012) 3653–3660.

[30] J. Zhang, F.H.B. Lima, M.H. Shao, K. Sasaki, J.X. Wang, J. Hanson, R.R. Adzic, Platinum monolayer on nonnoble metal−noble metal core−shell nanoparticle electrocatalysts for O2 reduction, J. Phys. Chem. B 109 (48) (2005) 22701–22704.

[31] L. Zhang, R. Iyyamperumal, D.F. Yancey, R.M. Crooks, G. Henkelman, Design of Pt-shell nanoparticles with alloy cores for the oxygen reduction reaction, ACS Nano 7 (10) (2013) 9168–9172.

[32] A. Dhouib, H. Guesmi, DFT study of the M segregation on MAu alloys (M=Ni, Pd, Pt) in presence of adsorbed oxygen O and O2, Chem. Phys. Lett. 521 (2012) 98–103.

[33] J.R. Kitchin, J.K. Nørskov, M.A. Barteau, J.G. Chen, Role of strain and ligand effects in the modification of the electronic and chemical properties of bimetallic surfaces, Phys. Rev. Lett. 93 (15) (2004) 156801.

[34] M. Mavrikakis, B. Hammer, J.K. Nørskov, Effect of strain on the reactivity of metal surfaces, Phys. Rev. Lett. 81 (13) (1998) 2819–2822.

[35] J. Cho, S. Lee, J. Han, S.P. Yoon, S.W. Nam, S.H. Choi, K.-Y. Lee, H.C. Ham, Importance of ligand effect in selective hydrogen formation via formic acid decomposition on the bimetallic Pd/Ag catalyst from first-principles, J. Phys. Chem. C 118 (39) (2014) 22553–22560.

[36] H.C. Ham, D. Manogaran, K.H. Lee, K. Kwon, S.-a. Jin, D.J. You, C. Pak, G.S. Hwang, Communication: enhanced oxygen reduction reaction and its underlying mechanism in Pd-Ir-Co trimetallic alloys, J. Chem. Phys. 139 (20) (2013) 201104.

[37] G. Henkelman, A. Arnaldsson, H. Jonsson, A fast and robust algorithm for Bader decomposition of charge density, Comp. Mater. Sci. 36 (3) (2006) 354–360.

[38] C. Wang, M. Chi, D. Li, D. Strmcnik, D. van der Vliet, G. Wang, V. Komanicky, K.-C. Chang, A.P. Paulikas, D. Tripkovic, J. Pearson, K.L. More, N.M. Markovic, V.R. Stamenkovic, Design and synthesis of bimetallic electrocatalyst with multilayered Pt-Skin surfaces, J. Am. Chem. Soc. 133 (36) (2011) 14396–14403.

[39] G. Wang, B. Huang, L. Xiao, Z. Ren, H. Chen, D. Wang, H.D. Abruña, J. Lu, L. Zhuang, Pt skin on AuCu intermetallic substrate: a strategy to maximize Pt utilization for fuel cells, J. Am. Chem. Soc. 136 (27) (2014) 9643–9649.

[40] D. Segets, J.M. Lucas, R.N. Klupp Taylor, M. Scheele, H. Zheng, A.P. Alivisatos, W. Peukert, Determination of the quantum dot band gap dependence on particle size from optical absorbance and transmission electron microscopy measurements, ACS Nano 6 (10) (2012) 9021–9032.